Supporting Information

S1. CFD simulation setup and numerical methods

A simplified three-dimensional model of the study hexacopter was constructed, comprising the central fuselage and six rotor forcing regions. The arms, landing gear, and other small components were omitted. The rotor diameter was 0.62 m, with adjacent and opposite motor centres separated by 0.80 and 1.60 m, respectively. The simulation represented windless hovering at an assumed representative total mass of 10 kg, without ground effects. Each rotor was represented by a finite-thickness actuator volume with a uniformly distributed downward force integrating to 16.35 N, giving a total force equal to the aircraft weight.

Simulations were performed using COMSOL Multiphysics 6.3, solving the transient incompressible Navier–Stokes equations using a laminar-flow formulation. Air density and dynamic viscosity were set to 1.225 kg m^{-3} and 1.81 × 10^{-5} Pa s, respectively. The computational domain measured 6 × 6 × 17 m. All external boundaries were assigned open conditions at zero gauge pressure, while the fuselage surface was treated as a solid wall. A physics-controlled tetrahedral mesh containing 36,258 elements was used, without separately prescribed local refinement. The simulation covered 0–2.5 s, with results exported at 0.05 s intervals. Velocity magnitude was visualized using side-view and top-view maximum-value projections. Formal mesh-independence testing was not performed; the simplified calculation was used to inform inlet placement qualitatively.

Previous studies demonstrate the importance of considering platform geometry and rotor-induced airflow when positioning UAV sampling inlets (Crazzolara et al., 2019; Eckert et al., 2026). Particle transport through sampling lines introduces an additional design consideration because diffusion, sedimentation, and inertial deposition depend on particle size, tubing geometry, and flow conditions (von der Weiden et al., 2009). The selected inlet was positioned 0.60 m above the fuselage top, within a region of comparatively weak simulated airflow disturbance. Although this

was not the minimum-velocity location, the placement balanced separation from the rotors, the need to avoid unnecessarily extending the sampling line, and mounting feasibility. Together, the simulated flow pattern and published inlet configurations (Table S4) informed the practical inlet arrangement adopted for the field comparisons. The simplified simulation informed inlet placement, while the rotor comparisons evaluated measurement responses under the actual field conditions.

S2. The classification of individual particles

Individual aerosol particles were classified into four categories, S-rich, soot-containing, OM-containing, and Other, based on their TEM morphology and EDS elemental composition. Soot was identified by its characteristic aggregates of carbonaceous primary spheres, typically forming chain-like or compact structures. Particles with identifiable soot structures, whether largely exposed or associated with other components, were classified as soot-containing. S-rich particles were characterized by prominent S and O signals and frequently exhibited rounded outlines. OM-containing particles were identified from the combined evidence of their morphology and C- and O-rich composition, with organic material occurring as near-spherical particles or coatings.

The Other category comprised mineral, metal-containing, and sea-salt particles. Mineral particles generally exhibited irregular shapes and contained Si, Al, and O. Metal-containing particles were identified by prominent signals of metallic elements, such as Fe, whereas sea-salt particles were characterized by Na-rich compositions, commonly accompanied by Cl and/or Mg. Representative TEM images of the particle categories are shown in Fig. 4, and corresponding EDS spectra are provided in Fig. S4.

Soot-containing particles were further classified as bare-like, partly-coated, or embedded-coated based on the visible relationship between soot aggregates and surrounding material in TEM images. Bare-like soot exhibited little or no visible coating, whereas partly-coated and embedded-coated soot were partially and completely enclosed by other aerosol components, respectively.

S3. Calculation of concentration ratios and relative differences

The 1 s $PM_{2.5}$, BC, and POPS records obtained during the rotor comparisons were aggregated into non-overlapping 1 min intervals. For each measurement event, the arithmetic mean and standard deviation (SD) were calculated from the 1 min averages under each rotor condition. The SD describes temporal variability within each sampling period. Differences between rotor states were quantified using the mean minute-wise rotor-on/rotor-off concentration ratio (Rx) and relative difference (△X), with rotor-off measurements serving as the reference:

$$r_{X,i} = \frac{X_{on,i}}{X_{off,i}} \tag{S1}$$

$$R_x = \frac{1}{n}\sum_{i=1}^{n} r_{x,i} \tag{S2}$$

$$\triangle X = \frac{\bar{X}_{on} - \bar{X}_{off}}{\bar{X}_{off}} \times 100\% \tag{S3}$$

where $X_{on,\,i}$ and $X_{off,\,i}$ denote the 1 min mean concentrations at the same elapsed-minute index within the respective rotor-on and rotor-off periods, and n is the number of valid minute-wise ratios. $\bar{X}_{on}$ and $\bar{X}_{off}$ denote the arithmetic means of the 1 min values obtained during the rotor-on and rotor-off stages, respectively. Here, X represents $PM_{2.5}$, BC, total particle number concentration (PNC), or size-resolved PNC.

The 95% confidence interval for the mean minute-wise ratio was calculated as

$$R_X \pm t_{0.975,n-1}\frac{s_r}{\sqrt{n}}$$

where S_r is the sample standard deviation of the minute-wise ratios and n is the number of valid ratios.

For the ratio comparisons, 1 min mean concentrations from the rotor-on and rotor-off periods were matched by elapsed-minute index, and their ratios were calculated. The reported ratio and its 95% confidence interval represent the arithmetic mean of these minute-wise ratios and the confidence interval for that mean, respectively. The confidence intervals were calculated without adjustment for temporal autocorrelation.

S4. Calculation of particle morphology parameters

AR and SC were calculated from the two-dimensional projections of all analyzed particles:

$$\mathrm{AR} = \max\left(\frac{\mathrm{L}}{\mathrm{W}}\right) \tag{S4}$$

$$\mathrm{SC} = \frac{\mathrm{R_{inscribing}}}{\mathrm{R_{circumscribing}}} \tag{S5}$$

where L and W denote the projected particle length and the corresponding perpendicular width, respectively. $\mathrm{R_{inscribing}}$ and $\mathrm{R_{circumscribing}}$ are the radii of the inscribed and circumscribed circles centred on the centroid of the particle projection, respectively. The geometric definitions are illustrated in Fig. S5.

Figures

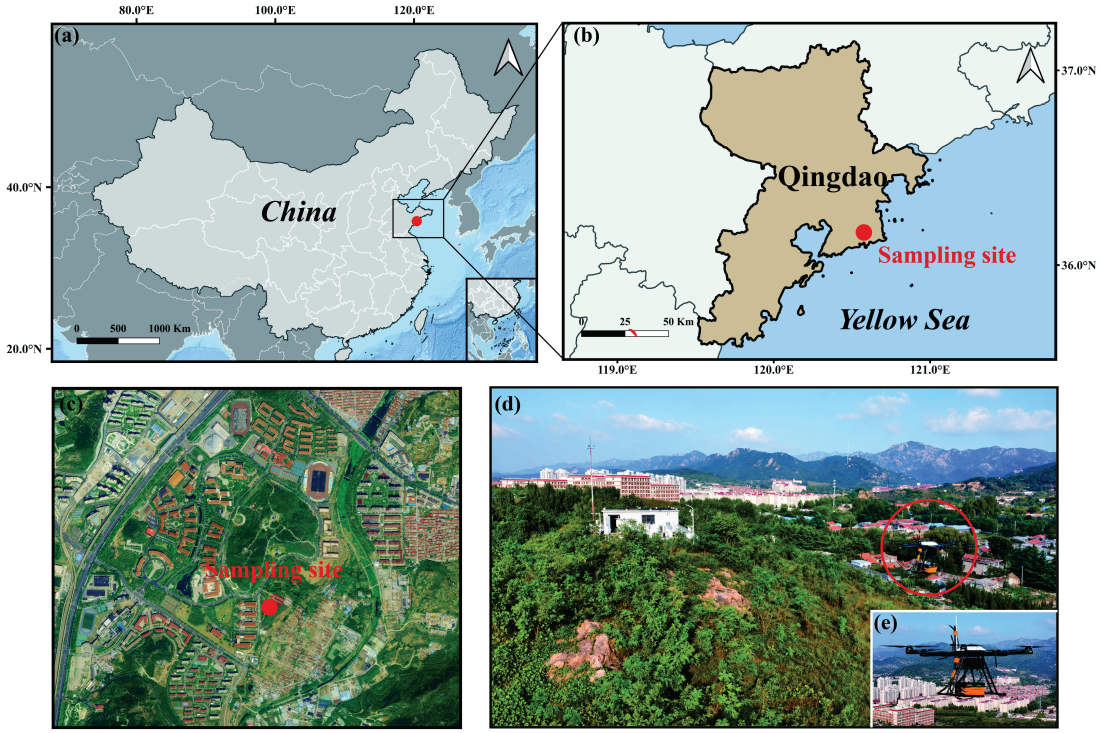

Figure S1. Sampling location and field deployment of the UAV platform. (a) Location of Qingdao in China. (b) Sampling site within Qingdao. (c) Satellite image of the sampling site. (d) Field view of the sampling area and hovering UAV. (e) Close-up view of the UAV platform. Red markers indicate the sampling site in (a–c), and the red circle identifies the UAV in (d).

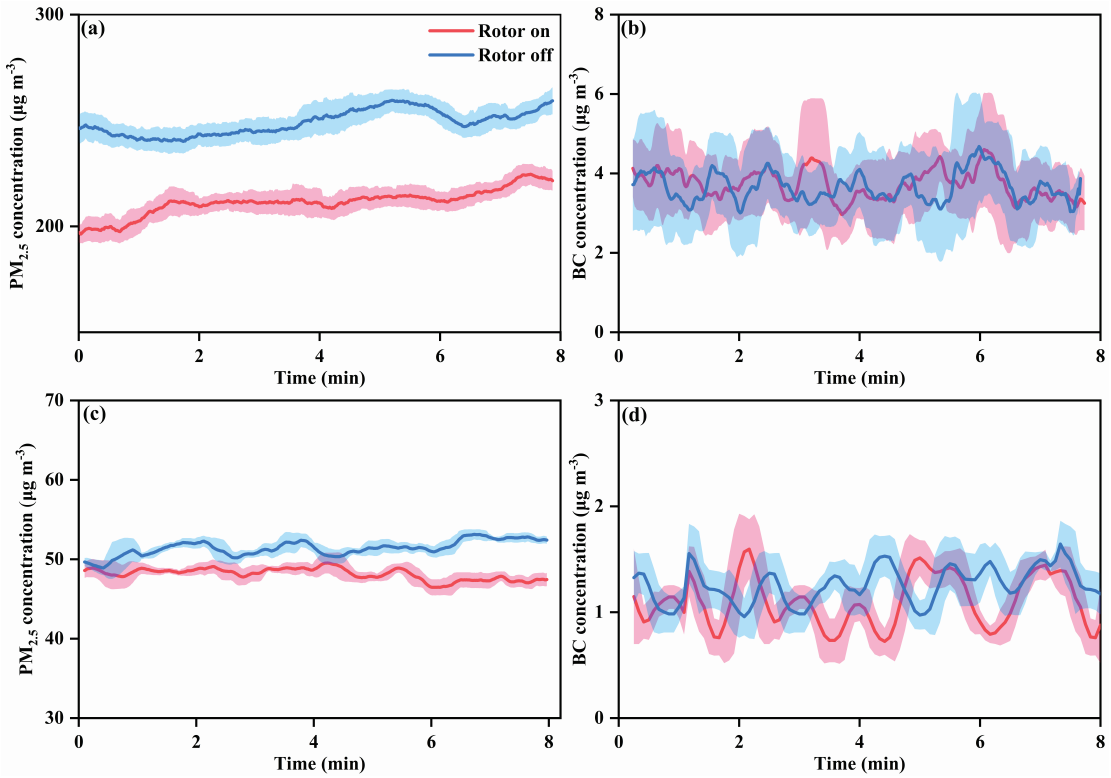

Figure S2. Time series of $PM_{2.5}$ and BC mass concentrations during the rotor comparisons under polluted (a, b) and clean (c, d) conditions. (a, c) show $PM_{2.5}$, and panels (b, d) show BC. Red and blue lines represent rotor-on and rotor-off measurements, respectively. Time denotes elapsed time from the start of each measurement period. Lines show 60 s moving averages, and shaded bands indicate ±1 sample SD within each moving window. These moving-window statistics are used for visualization; the quantitative comparisons are based on non-overlapping 1 min averages.

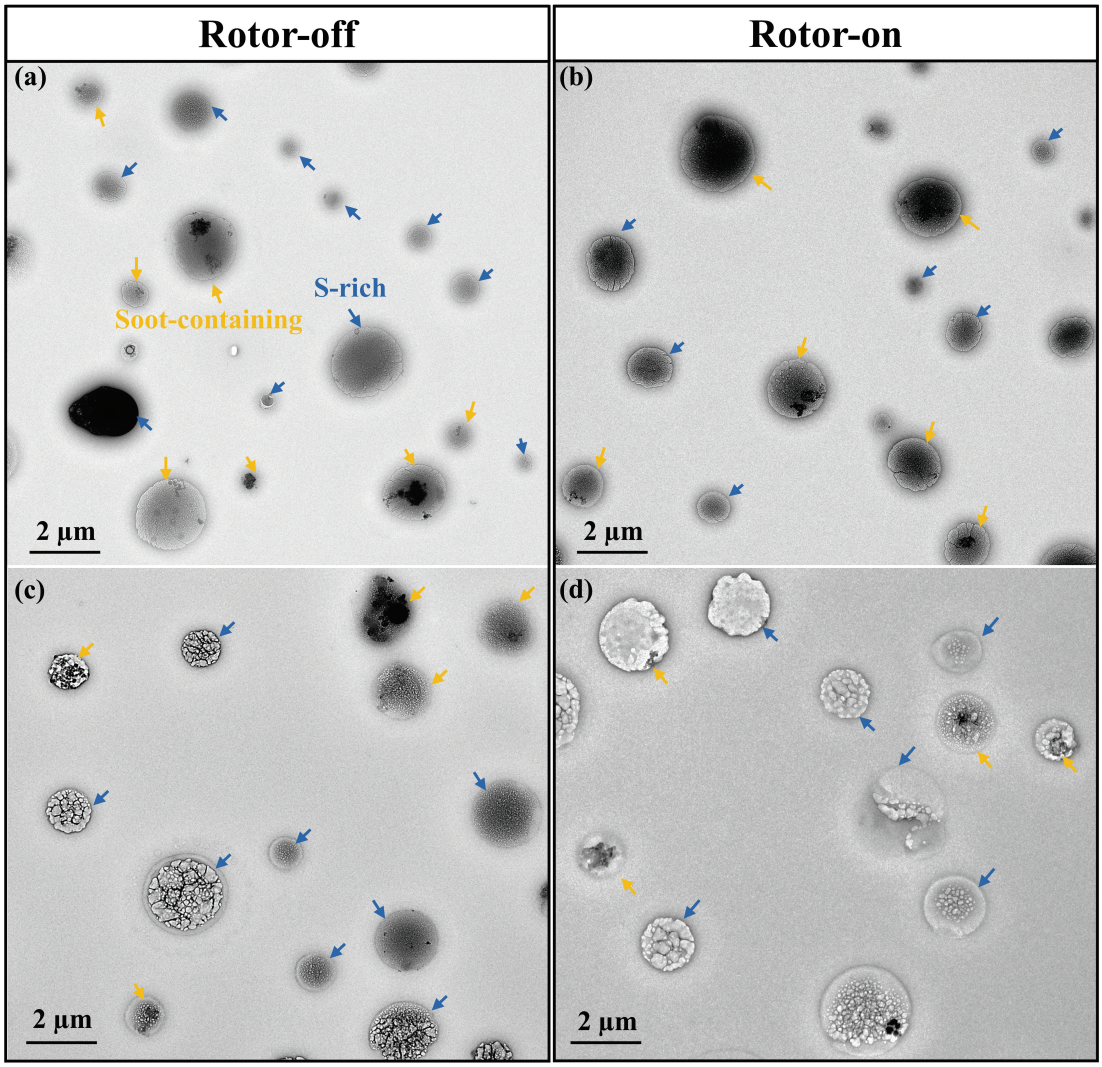

Figure S3. Representative low-magnification TEM images of individual aerosol particles collected under polluted (a, b) and clean (c, d) conditions. (a, c) show rotor-off samples, and (b, d) show rotor-on samples. Yellow and blue arrows indicate soot-containing and S-rich particles, respectively.

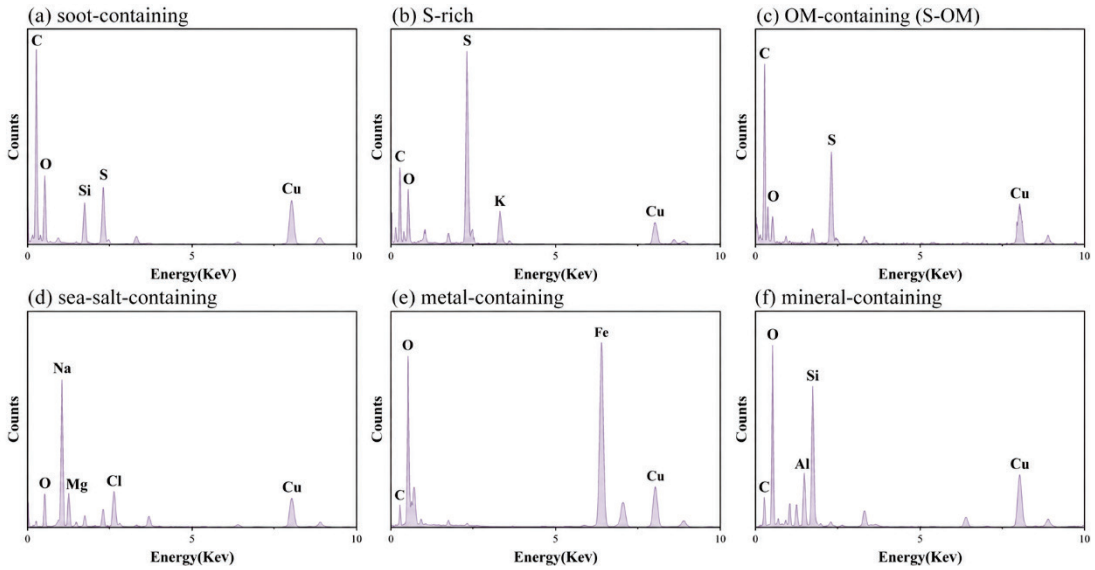

Figure S4. Representative energy-dispersive X-ray spectroscopy (EDS) spectra of (a) soot-containing, (b) S-rich, (c) OM-containing (S–OM), (d) sea-salt-containing, (e) metal-containing, and (f) mineral-containing particles.

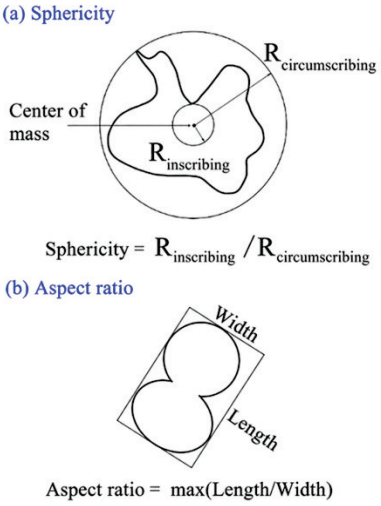

Figure S5. The diagrams and equations of (a) Sphericity (SC), and (b) Aspect Ratio (AR).

Tables

Table S1. Sampling information and meteorological conditions during the rotor comparison campaigns.

Parameter	6 January 2026	21 March 2026	15 June 2026
Pollution condition	Polluted	Clean	Clean
Measurements / sampling	$PM_{2.5}$, BC, and individual particles	$PM_{2.5}$ and BC; POPS measurements in a separate flight	Individual particles
Sampling period	15:00–16:00	15:00–16:00	15:00–16:00
Air temperature (°C)	5.6	9.8–10.2	23.0–23.2
Relative humidity (%)	60–62	76–78	75–76
Wind speed (m s^{-1})	4.29–4.87	6.65–6.80	3.83–4.07
Wind direction (°)	253–262	179–180	138–140

Table S2. Sampling information, meteorological conditions, and daily mean particulate matter concentrations during the vertical profiling campaigns.

Parameter	16 January 2026	18 January 2026
Pollution condition	Polluted	Clean
Sampling time (Beijing time, UTC+8)	09:00	09:00
Air temperature (°C)	6.8	0.4
Relative humidity (%)	81	79
Wind speed (m s^{-1})	3.37	5.98
Wind direction (°)	238	48
Daily mean $PM_{2.5}$ (μg m^{-3})	81	15
Daily mean PM_{10} (μg m^{-3})	157	25

Table S3. Summary statistics of aspect ratio (AR) and sphericity (SC) for individual particles collected under rotor-on and rotor-off conditions during the polluted and clean campaigns.

Campaign	Rotor state	n	AR, mean ± SD	AR, median (Q1–Q3)	SC, mean ± SD	SC, median (Q1–Q3)
Polluted	On	262	1.112 ± 0.110	1.080 (1.060–1.130)	0.842 ± 0.129	0.880 (0.800–0.930)
Polluted	Off	257	1.133 ± 0.201	1.090 (1.060–1.130)	0.828 ± 0.142	0.870 (0.790–0.920)
Clean	On	229	1.122 ± 0.122	1.090 (1.060–1.130)	0.832 ± 0.133	0.860 (0.800–0.910)
Clean	Off	231	1.117 ± 0.105	1.090 (1.070–1.130)	0.838 ± 0.118	0.860 (0.800–0.920)

Table S4. Inlet positions and mounting configurations in previous UAV-based aerosol studies.

UAV platform	Inlet / sensor position	Target measurement	Assessment method	Reference
DJI Matrice 200 V2 Quadcopter	POPS below the fuselage; inlet extended 0.20 m above the rotors.	PNC and particle size distribution	Ground measurements with rotors stopped and operating; hovering at 10 m.	Liu et al. (2021)
Meteodrone MM-670 Hexacopter	POPS below the UAV; inlet bent upwards and extended 0.05 m above rotor level.	PNC and particle size distribution	Hovering versus stationary rotor-off measurements; comparison with a reference POPS on a tethered balloon.	Miller et al. (2024)
DJI M600 Hexacopter	OPC approximately 1.00 m above the rotor plane, with an upward-facing inlet and no additional inlet tube; anemometer at 1.10 m.	PNC, size distribution, PM, BC, trace gases, and meteorology	Mounting-height assessment and characterization of measurement uncertainty and flight-motion effects.	Moormann et al. (2025)
Custom-built UAV Quadcopter	Vertical sampling inlet 0.36 m in height, connected through a splitter and dehumidifier; tube height is not a rotor-plane separation.	PM_1, $PM_{2.5}$, and PM_{10}	Comparisons with a stationary reference, with and without the sampling inlet.	Ahlawat et al. (2026)
UH-AeroSAM Octocopter	Open-path OPC above the airframe, within an annulus 0.15–0.20 m radially from the centre; this is a radial location, not an inlet height.	Particle and cloud-droplet size distributions	CFD with Lagrangian particle tracking; field comparison with a reference cloud probe.	Girdwood et al. (2020)
DJI M600 Hexacopter	Body-mounted sampling compared with sampling on vertical or horizontal extension arms beyond the rotors.	$PM_{2.5}$, CO, and CO_2	Paired instrument comparisons in laboratory and biomass-burning field tests.	Aurell and Gullett (2024)

References

Ahlawat, A., Julaha, K., Tiwari, P., Deshmukh, S., Atabakhsh, S., Bran, S. H., Baig, N. A., Balyan, P., Mandariya, A. K., Ganguly, D., Karatzas, K., Kumar, M., Singh, V., Khaiwal, R., Kumar, P., Biskos, G., Sun, Y., Wehner, B., Dey, S., and Pöhlker, M.: Drone measurements reveal high near-surface urban haze, npj Clean Air, 2, 8, https://doi.org/10.1038/s44407-025-00044-3, 2026.

Aurell, J. and Gullett, B. K.: Effects of UAS rotor wash on air quality measurements, Drones, 8, 73, https://doi.org/10.3390/drones8030073, 2024.

Crazzolara, C., Ebner, M., Platis, A., Miranda, T., Bange, J., and Junginger, A.: A new multicopter-based unmanned aerial system for pollen and spores collection in the atmospheric boundary layer, Atmos. Meas. Tech., 12, 1581–1598, https://doi.org/10.5194/amt-12-1581-2019, 2019.

Eckert, C., Tong, F., Harrison, D. P., and Kelaher, B. P.: Quantifying drone propeller-induced flow for optimal aerosol sensor placement, Phys. Fluids, 38, 015179, https://doi.org/10.1063/5.0310240, 2026.

Girdwood, J., Smith, H., Stanley, W., Ulanowski, Z., Stopford, C., Chemel, C., Doulgeris, K.-M., Brus, D., Campbell, D., and Mackenzie, R.: Design and field campaign validation of a multi-rotor unmanned aerial vehicle and optical particle counter, Atmos. Meas. Tech., 13, 6613–6630, https://doi.org/10.5194/amt-13-6613-2020, 2020.

Liu, Z., Osborne, M., Anderson, K., Shutler, J. D., Wilson, A., Langridge, J., Yim, S. H. L., Coe, H., Babu, S., Satheesh, S. K., Zuidema, P., Huang, T., Cheng, J. C. H., and Haywood, J.: Characterizing the performance of a POPS miniaturized optical particle counter when operated on a quadcopter drone, Atmos. Meas. Tech., 14, 6101–6118, https://doi.org/10.5194/amt-14-6101-2021, 2021.

Miller, A. J., Ramelli, F., Fuchs, C., Omanovic, N., Spirig, R., Zhang, H., Lohmann, U., Kanji, Z. A., and Henneberger, J.: Two new multirotor uncrewed aerial vehicles (UAVs) for glaciogenic cloud seeding and aerosol measurements within the CLOUDLAB project, Atmos. Meas. Tech., 17, 601–625, https://doi.org/10.5194/amt-17-601-2024, 2024.

Moormann, L., Böttger, T., Schuhmann, P., Valero, L., Fachinger, F., and Drewnick, F.: The Flying Laboratory FLab: Development and application of a UAS to measure aerosol particles and trace gases in the lower troposphere, Atmos. Meas. Tech., 18, 1441–1459, https://doi.org/10.5194/amt-18-1441-2025, 2025.

von der Weiden, S.-L., Drewnick, F., and Borrmann, S.: Particle Loss Calculator – a new software tool for the assessment of the performance of aerosol inlet systems, Atmos. Meas. Tech., 2, 479–494, https://doi.org/10.5194/amt-2-479-2009, 2009.